Hydrodynamic modelling of tidal-fluvial flows in a large river estuary

Sandbach, S.D.[a,b,1], Nicholas, A.P.[a], Ashworth, P.J.[b], Best, J.L.[c,d], Keevil C.E. [e], Parsons, D.R.[e], Prokocki, E.W.[d], Simpson, C.J.[b]

[a]*Department of Geography, University of Exeter, Exeter, EX4 4QJ, UK*

[b]*Division of Geography and Geology, School of Environment and Technology, University of Brighton, Brighton, Sussex, BN2 4GJ, UK*

[c]*Departments of Geology, Geography and Geographic Information Science, Mechanical Science and Engineering and Ven Te Chow Hydrosystems Laboratory, University of Illinois at Urbana-Champaign, 605 East Springfield Avenue, Champaign IL, 61820, USA*

[d]*Department of Geology, University of Illinois at Urbana-Champaign, 1301 W. Green St., Urbana, IL, 61801, USA.*

[e]*Department of Geography, Environment and Earth Sciences, University of Hull, Hull, HU6 7RX, UK*

[1]*Corresponding author's present address: Met Office, FitzRoy Road, Exeter, Devon, EX1 3PB, United Kingdom, steven.sandbach@metoffice.gov.uk*

Keywords: Sediment transport, tidal constituent, residual flow, tidal-fluvial interactions, Columbia River Estuary, model parameterisation.

Abstract

The transition between riverine and estuarine environments is characterised by a transition from unidirectional to bidirectional flows, in a region referred to herein as the Tidally-Influenced Fluvial Zone (TIFZ). In order to improve our understanding of the hydrodynamics and morphodynamics of this zone, we present a combined field and numerical modelling study of the Columbia River Estuary (CRE), USA, tidally-influenced fluvial zone. The CRE is large measuring 40 km in length and between 5 and 10 km wide. A shallow water model (Delft3D) was applied in both 2D and 3D configurations and model sensitivity to the key process parameterizations was investigated. Our results indicate that a 2D model constrained within the estuary can sufficiently reproduce depth-averaged flow within the TIFZ of a stratified estuary.

Model results highlight the interactions between tidal-, fluvial- and topographic-forcing that result in depth dependent tidal rectification, and thus zones of residual sediment transport that: i) may be flood-directed along shallow channel margins and in the lee of bars, and simultaneously ii) is ebb-directed within deeper channel thalwegs. This condition is enhanced at lower discharges, but increased fluvial discharge reduces the number and size of regions with net flood-directed sediment transport and flow. These sediment transport patterns provide a mechanism to extend the bar/island topography downstream, and generate flood-directed, ebb-directed, and symmetrical bedforms, all within the same channel. Analysis of the model data reveals flood-directed sediment transport is due to both tidal variability and mean flow. These results highlight the need to include the mean flow component (M_0) when considering the long-term morphodynamic evolution in a TIFZ.

1. Introduction

Tidally-influenced fluvial zones (TIFZs) represent some of the most complex environments on Earth [Dalrymple and Choi, 2007], and extend from the mouth of an estuary, or delta, through the freshwater tidal river reach, whose landward limit terminates at the most upstream point of observable variations in water surface elevations caused by tidal-flows [Hoitink and Jay 2016]. TIFZs are commonly sub-divided into three general hydraulic zones defined by the mean ratio of tidal *vs* fluvial energy input, and include [see Jay et al. 1990; Jablonski and Dalrymple 2016]: i) tidally-dominated lower river (i.e., estuary), ii) tidally-dominated, fluvially-influenced, or mixed tidal-fluvial regime, and iii) fluvially-dominated, tidally-influenced regime. Thus, it is at the boundary between the tidally-dominated lower TIFZ, or brackish water upper estuary, and the mixed tidal-fluvial regime (downstream boundary of freshwater tidal river reach; middle TIFZ), where tidal-flows are strongly impacted by varying river discharges, bed geometry/bathymetry, and water density [Jay and Smith, 1988]. These factors drive asymmetric hydrodynamic flows with either flood- or ebb-dominance [Dyer 1997, chapter 2], and associated net sediment transport [Guo et al., 2014], and are referred to as tidal rectification [cf. Huthnance 1973; Bowers and Al-Barakati 1997].

The hydrodynamics and morphodynamics in tidally–dominated estuaries have been well studied [cf. Guo et al., 2014; Zhou et al., 2014; Chu et al., 2015; Guo et al., 2016], with net sediment transport related to: i) tidal velocity asymmetries [Van Maren et al., 2004; Díez-Minguito et al., 2012; Guo et al., 2014]; ii) the generation of the M_4 overtide [Friedrichs and Aubrey, 1988]; and iii) the triad interaction M_2-O_1-K_1 [Hoitink et al.,

2003]. The focus of recent work on the middle to upper TIFZ includes suspended sediment dynamics [Achete et al., 2016], interactions between mean and tidal flow components [Van Maren et al., 2004; Chu et al., 2015], net water transport [Alebregtse and de Swart, 2016], and determination of the relative importance of non-stationary river vs stationary tidal energy signals in governing streamwise fluctuations in the water surface elevation [Matte et al., 2013; Guo et al., 2015; Jay et al., 2015], and/or flow velocity magnitudes and orientations [Losada et al., 2017].

A number of process-based hydraulic models have been applied to study the Columbia River Estuary (CRE) [Kärnä and Baptista, 2016], including the Regional Ocean Modeling System [Liu et al., 2009], ELCIRC [Zhang et al., 2004], SELFE [Zhang and Baptista, 2008] and Delft3D [Elias et al., 2012]. The predominant focus of these model applications has been on plume dynamics and estuary mouth processes. Because of this focus, the impact of stratification was important and thus these models were all deployed in 3D mode.

Modelling studies of other estuaries include 3D [e.g. Burla et al., 2010] and 2D [e.g. Bolle et al., 2010; Prario et al., 2011] representations. In most cases, the modelling domains include the estuary mouth and so apply a coastal boundary condition. Notable exceptions are Prario et al. [2011] and Matte et al. [2017a, 2017b], who constrained their models to within the estuary. This suggests that it may be possible to apply a 2D model to the TIFZ of the CRE. Herein, we test this by applying both 2D and 3D simulations with the model boundary located both inside and outside the estuary.

Despite this recent interest, little is known about TIFZ channel scale hydrodynamics and morphodynamic processes that determine how channels and sand bars evolve, which ultimately are one of the important sedimentological building blocks of estuaries and deltas [Dalrymple and Choi, 2007; Leuven et al., 2016]. Therefore, to investigate TIFZ channel to barform evolution, a combined field and numerical modelling study was conducted on the meso-tidal lower Columbia River (LCR), WA/OR, USA [Prokocki et al. 2015].

Thus, in this paper three principal questions are addressed:

1. Can a 2D model be used to simulate accurately the LCR TIFZ (i.e., estuary) where density stratification is present?
2. What are the dominant characteristics of LCR TIFZ channel scale hydrodynamics and morphodynamics, and how do these processes affect bedform to barform evolution?
3. How do fluctuations between low- and high-river flow impact LCR TIFZ bedform to barform evolution?

To address these points, a modelling study of the LCR TIFZ including different levels of process representation to evaluate the impacts of waves, 3D/2D, boundary location, and bedform roughness and turbulent viscosity, is developed herein. Details of the modelling setup are provided in section 3. The model that performed best was assessed by calibration, using measured water level data, and validation with other hydrodynamic data (sections 4.1 and 4.2). Results from the best performing model were then used to investigate channel-scale hydrodynamics and morphodynamics within the

LCR TIFZ (section 4.3). Due to the large variability in river-discharge, the effect of flow discharge on model calibration/validation and channel scale process was also analysed.

2. Columbia River Estuary

The Columbia River is the largest river entering the Pacific Ocean from North America, with an average river-discharge of ~7300 m^3 s^{-1} [Jay et al., 2010]. The discharge is seasonally variable with a typical minimum autumn-early spring flow of ~3000 m^3 s^{-1} and a spring freshet between 10,000 to 15,000 m^3 s^{-1}. The tide is mixed diurnal and semidiurnal with a tidal range of 3.6-4 m [Fain et al., 2001]. Within the Columbia River littoral cell, the wave climate is seasonally-variable and high-energy with significant wave heights H_s = 3 m and peak period T_p = 12 s in the winter season [Gelfenbaum and Kaminsky, 2010]. A deep thalweg (Navigation Channel), which is periodically dredged, meanders through the central portion of the estuary flanked to the north and south by embayments (Figure 1).

2.1 Data availability

Bathymetric and topographic measurements from various sources and time periods are available offshore and within the estuary. The National Oceanic and Atmospheric Administration (NOAA) collected Multi-Beam Echo Sounding (MBES) data predominantly within the Navigation Channel stretching from the mouth to river-mile 18 (2007), river-mile 18 to 25 (2008), river-mile 25 to 28.5 (2011) and from river-mile 28.5 to Beaver Army Terminal (2009). Areas outside the Navigation Channel were

143 surveyed using Single-Beam Echo Sounding (SBES) by the United States Army Corps of
144 Engineers (USACE) in 2003 and 2009. Shallow areas inaccessible to the USACE vessels
145 were surveyed using SBES in 2009 and 2010 by the Lower Columbia River Estuary
146 Partnership (LCREP). Exposed topography within the estuary was measured by Light
147 Detection and Ranging (LiDAR) in 2005 by the Puget Sound LiDAR Consortium (PSLC).
148 Just outside the estuary mouth, NOAA (2007) and USACE (2009) conducted MBES
149 bathymetric surveys. For the remainder of the coastal zone, 20 km north and south and
150 40 km west of the mouth, data collected by NOAA using a fathometer during the 1920s
151 and 1950s are also available.
152

Figure 1: Aerial photography of the lower Columbia River Estuary showing (A) modelling domain location and boundaries and, (B) ADCP cross-section locations. Model grid resolution has been reduced by a factor of 8 for clarity. Aerial photographs (2009) provided courtesy of the United States Department of Agriculture National Agriculture Imagery Program.

Gauging stations maintained by NOAA and CMOP (Coastal Margin Observation & Prediction) are present throughout the system, collecting both hydrological and biological data. Hydrological data monitored in the estuary include water surface

elevation, salinity, temperature, wave climate and discharge. The data used in this paper were obtained from CMOP (http://www.stccmop.org), NOAA (http://www.noaa.gov) and USGS (http://waterdata.usgs.gov). The locations of the gauging stations are shown in Figure 1A.

2.2 Flow surveys

Flow data were obtained using a Teledyne RD Instruments 1200 kHz ADCP deployed from a small inflatable boat, which was set to determine three-dimensional flow in a vertical column at 0.25 m interval bins at a rate of ~1 Hz. The ADCP was deployed in moving-boat mode with vessel position and velocity correction provided via Real Time Kinematic GPS. The distance from the water surface to the first ADCP measurement bin was 0.91 m, which accounted for submergence of the ADCP below the water-line and the blanking distance that removes the effect of acoustic ringing [Szupiany et al., 2007]. Data from the bottom 6% of the profile were also removed in processing, to remove the effect of contamination by side-lobe interference. Due to the large length scales and short time-scales for survey data collection, it was not possible to take repeat measurements for stable flow conditions. Therefore, in this paper, velocity data are depth-averaged to remove non-stationary turbulent signals.

The average boat velocity during the surveys was 1.09 m s^{-1}, providing high-resolution (~6.3 measurements m^{-2}) velocity data along each cross-section. Seven transects were surveyed during the high river-discharge period (field seasons 1 and 3). A subset of these transects were re-surveyed during the low river-discharge period (field-season

2). The locations of all the surveyed transects are illustrated in Figure 1. The transects surveyed at low river flow are marked as dashed lines. The data were processed using the VMT Matlab toolbox [Parsons et al., 2013]. Raw and processed data files are available at: http://fluvialtidal.com.

The field survey collection periods ranged from 4 to 8 hours per deployment with an average of 5 hours depending on the prevailing conditions. Each transect was typically surveyed at least five times. The typical time for each survey was around 30 minutes but smaller channels could be crossed in 10 minutes while others took approximately an hour to survey. Processing of ADCP data using a time-interpolation method produced no perceptible difference in the spatial distribution of velocity.

3. Modelling simulations

3.1 Numerical model

Both 2D and 3D Delft3D-FLOW [Deltares 2011a] models were setup to simulate the Columbia River TIFZ. The horizontal momentum equations include forcing associated with: i) Coriolis force (model latitude ϕ = 46.1881°); ii) horizontal and vertical kinematic eddy viscosity ν_V and ν_H; iii) water-surface and bed shear stresses; and iv) pressure gradient forces expressed through the application of a hydrostatic pressure assumption.

Free surface and bedform shear stresses are included using the quadratic friction law: $\tau_b = \rho_{ref} C_d \vec{U}_{ref} \left| \vec{U}_{ref} \right|$, where τ_b is the shear stress, ρ_{ref} is the reference density, C_d is a drag coefficient and $\vec{U}_{ref}$ is the reference velocity. At the free-surface, the air density and wind velocity are used in this formulation and C_d varying between 0.0025 and 0.0289 [Elias et al., 2012]. For bed roughness effects, a slightly modified version of drag coefficient is used; the Chezy roughness parameter: $C = \sqrt{g/C_d}$. Also, in this case the water density and the near-bed (3D model) or depth-averaged (2D model) velocities are used $\left(\vec{U}_{ref}\right)$ in the shear stress parameterization.

The viscosity associated with vertical shear is: $\nu_v = \nu_{mol} + \max(\nu_{3D}, \nu_v^{back})$, where ν_{mol} is the molecular fluid viscosity, ν_{3D} is the 3D eddy-viscosity and ν_v^{back} is the vertical background eddy-viscosity. In the horizontal, the viscosity is: $\nu_H = \nu_v + \nu_H^{back} + \nu_{SGS}$; where ν_H^{back} is the user specified horizontal background eddy-viscosity and ν_{SGS} is the horizontal Sub-Grid-Scale (SGS) eddy-viscosity. The SGS terms are computed using the Uittenbogaard HLES (Horizontal Large Eddy Simulation) model [Deltares, 2011a, pp. 532-537]. A similar relationship holds for the diffusive terms (D_v and D_H) [Deltares, 2011a, pp. 203]. In the present paper, the background viscosity and diffusion are defined following Elias et al. [2012] whereby $\nu_H^{back} = D_H^{back} = 1$ m^2 s^{-1} and $\nu_v^{back} = D_v^{back} = 10^{-6}$ m^2 s^{-1}. The 3D viscosity and diffusion (ν_{3D} and D_{3D}) is computed using the k-ε turbulence model [Deltares, 2011a, pp. 231-233]. The cyclic advection scheme is used for both momentum and scalar transport.

232 In some of the simulations (Table 1), the hydrodynamic model was coupled with
233 Delft3D-WAVE (SWAN version 40.72ABCDE). The model parameterisation of Elias et al.
234 [2012] is used herein, including an overlapping WAVE grid.
235

Modelling periods and mean fluvial discharge					
Field season	Mean fluvial discharge ($m^3\ s^{-1}$)		Model period		
1	15,700		27/05/2011-27/06/2011		
2	4,200		15/09/2011-15/10/2011		
3	11,500		29/05/2012-29/06/2012		
Configurations					
Case	2D/3D	ν_H ($m^2 s^{-1}$)	Waves	C_{sea} ($m^{1/2}\ s^{-1}$)	C_{riv} ($m^{1/2}\ s^{-1}$)
1	3D	1.0	-	70	60
2	3D	1.0	Included	70	60
3	2D	1.0	-	60	60
4	2D	1.0	Included	60	60
5	2D	0.1	-	60	60
6	2D	10.0	-	60	65*
7	2D	HLES	-	60	65

236 **Table 1:** Modelled time periods and configurations assessed including a summary of the
237 optimal roughness parameters.
238

239 3.2 Model Application

240

241 3.2.1 Domains

Two domains were created (see Figure 1A). The first covered an area similar to the modelling domain used by Elias et al. [2012], and included the Columbia River (~30 km long and ~3 km wide), Estuary (~40 km long and ~5-10 km wide) and coastal zone (~40 km perpendicular and parallel to the shore). The second domain was a reduced version of the first, where the downstream boundary was moved from outside to inside the estuary (Figure 1A).

A variable resolution grid was used ranging from ~80 m in the estuary and up to 1000 m in the coastal region. In the 3D model simulations, the resolution was reduced by a factor of two to facilitate acceptable model run-times. The vertical resolution was greatest near the bed and free surface (4% of the depth) and lowest in the middle (17% of the depth), varying smoothly in-between over 10 layers. For the remainder of this paper, these domains are referred to as the sea-boundary and estuary-boundary domains respectively.

2D and 3D models were run in the estuary- and sea-boundary domains respectively. We initially tested a 2D model in the sea-boundary domain but the performance was poor. We choose not to implement a 3D model in the estuary-boundary domain because it was not possible to obtain accurate salinity boundary conditions.

3.2.2 Boundary conditions

The models were forced using discharge and water level boundary conditions. Water level data from Hammond tide gauge was used for the estuary-boundary simulations. An astronomical water level was specified at the western boundary of the domain in the sea-boundary simulations. The amplitude and phase of the nine components used were obtained from Elias et al. [2012].

The Local Mean Sea Level (LMSL) was specified using a conversion from NAVD88 to LMSL provided by NOAA's VDatum software (vdatum.noaa.gov). The water level boundary was supplemented with two zero-normal water level gradients (Neumann) at the north and south boundaries (Figure 1A). Time-series discharge observations obtained from the Beaver Army Terminal gauging station were used for the river boundary. This data includes the effects of both river- and tidal-forcing. The wind climate was specified using measured data from NOAA (NDBC buoy 46029) and the same parameterisation as Elias et al. [2012].

The salinity at the river and the sea boundaries during inflow were set equal to 0 and 33, respectively [Elias et al., 2012]. A Thatcher-Harleman time-lag [Deltares, 2011a] of 120 minutes was applied to provide smoothing.

3.2.3 Parameters

A series of model simulations were conducted to calibrate and assess model sensitivity. This assessment focused on: bed roughness; waves; model dimensionality; horizontal viscosity; and downstream boundary location.

The roughness values were specified spatially variable with: uniform roughness in the lower estuary and coastal domain (C_{sea}); uniform roughness in the river (C_{riv}); and a linear variation in the intervening region (see Figure 1A for transition points). This follows similar approaches by others [Baptista et al., 2005; Sassi et al., 2011; Elias et al., 2012; Van et al. 2016]. The range of values assessed was based on the values used in other studies of the CRE [Baptista et al., 2005; Elias et al., 2012].

A series of simulations were conducted using the baseline parameters described in section 3.2 for FLOW and FLOW-WAVE configurations. A further three model configurations were considered for the 2D estuary-boundary simulations where the horizontal background viscosity is varied (0.1, 10 $m^2\ s^{-1}$ and HLES). For each of these configurations, one-month long simulations were run (Table 1).

4. Results

4.1 Model calibration and sensitivity

The Mean Tidal Amplitude difference MTA_d = (MTA_m - MTA_o) and Mean Water Level difference MWL_d = (MWL_m - MWL_o) are used to calibrate the models. The subscript 'm' and 'o' indicate model predictions and observations. Figure 2 shows filled contour plots of MWL_d averaged across all available gauges for both field seasons two and three. The dotted line corresponds to the zero-contour for MTA_d (=MTA_{d0}). The optimal configuration is obtained where the zero-contour for both MWL_d (=MWL_{d0}) and MTA_d intersect. The 3D model over-predicts the MWL and so there is no zero-contour (Figures

2A and 2B). The results indicate that the model is more sensitive to tidal amplitude. For both sets of the 3D simulations, C_{riv} = 60 m½ s^{-1} and C_{sea} = 70 m½ s^{-1} provide optimal results [values are larger than Elias et al., 2012]. The optimal roughness values are summarised in Table 1.

The 3D sea-boundary model simulations (Figures 2A and 2B) show that the wave model increases the mean water level by around 0.025 m but has a negligible effect on tidal amplitude. In the 2D estuary-boundary simulations (Figures 2C with 2D) the wave model has a negligible effect but viscosity can lead to a significant shift in the tidal water levels (Figures 2C and 2F).

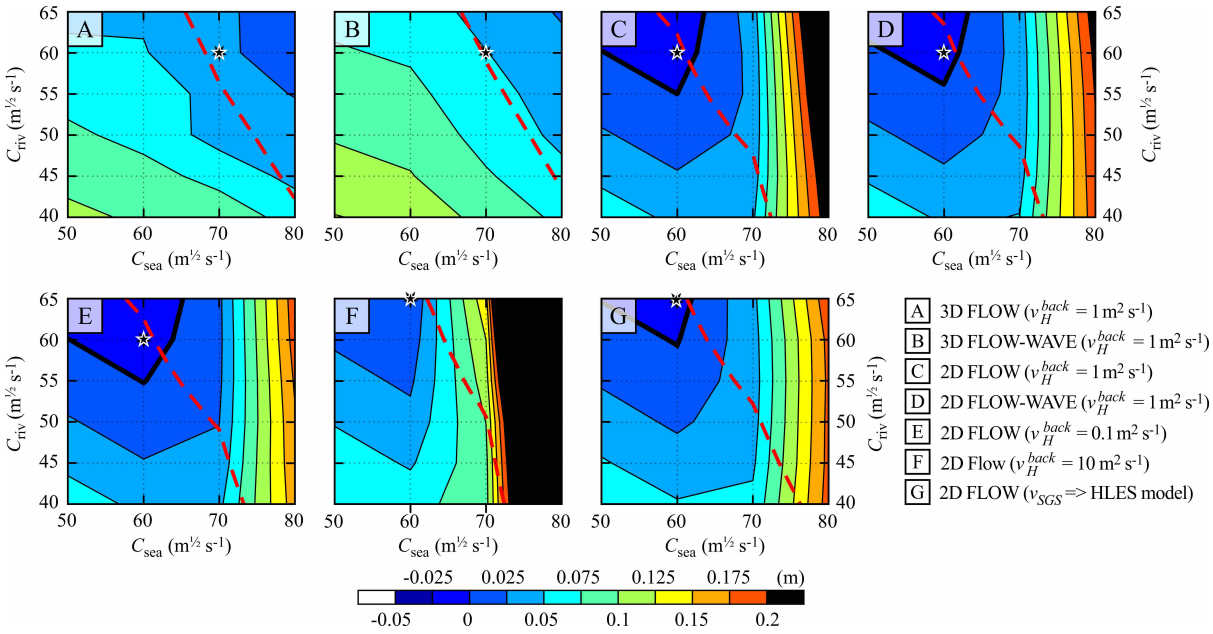

Figure 2: Filled contour plots of MWL_d averaged across all available gauges and river flow periods (field-seasons 2 and 3). Red dotted line is the zero-contour for MTA_d.

An inversion of the roughness sensitivity of the MWL metric to the sea roughness parameter is evident for the 3D model but not the 2D model (not shown). The mean high and low water levels (Figure 3A-D) show that the model is sensitive to the applied

330 C_{sea} at high water during low river-discharge, but insensitive during high-river-
331 discharge (Figures 3A and 3B). The reverse is true for the mean low water level (Figures
332 3C and 3D).
333
334 The response of the model at high and low water levels is related to flood and ebb
335 processes, and in particular to the work done by external forces. Considering only the
336 bed shear forcing ($F \propto U^2$), the work done W (=FUdt) may be computed and partitioned
337 into ebb (e) and flood (f) periods:
338
339 $$w_d = \left(W_e - W_f\right)/\left(W_e + W_f\right), \quad [1]$$

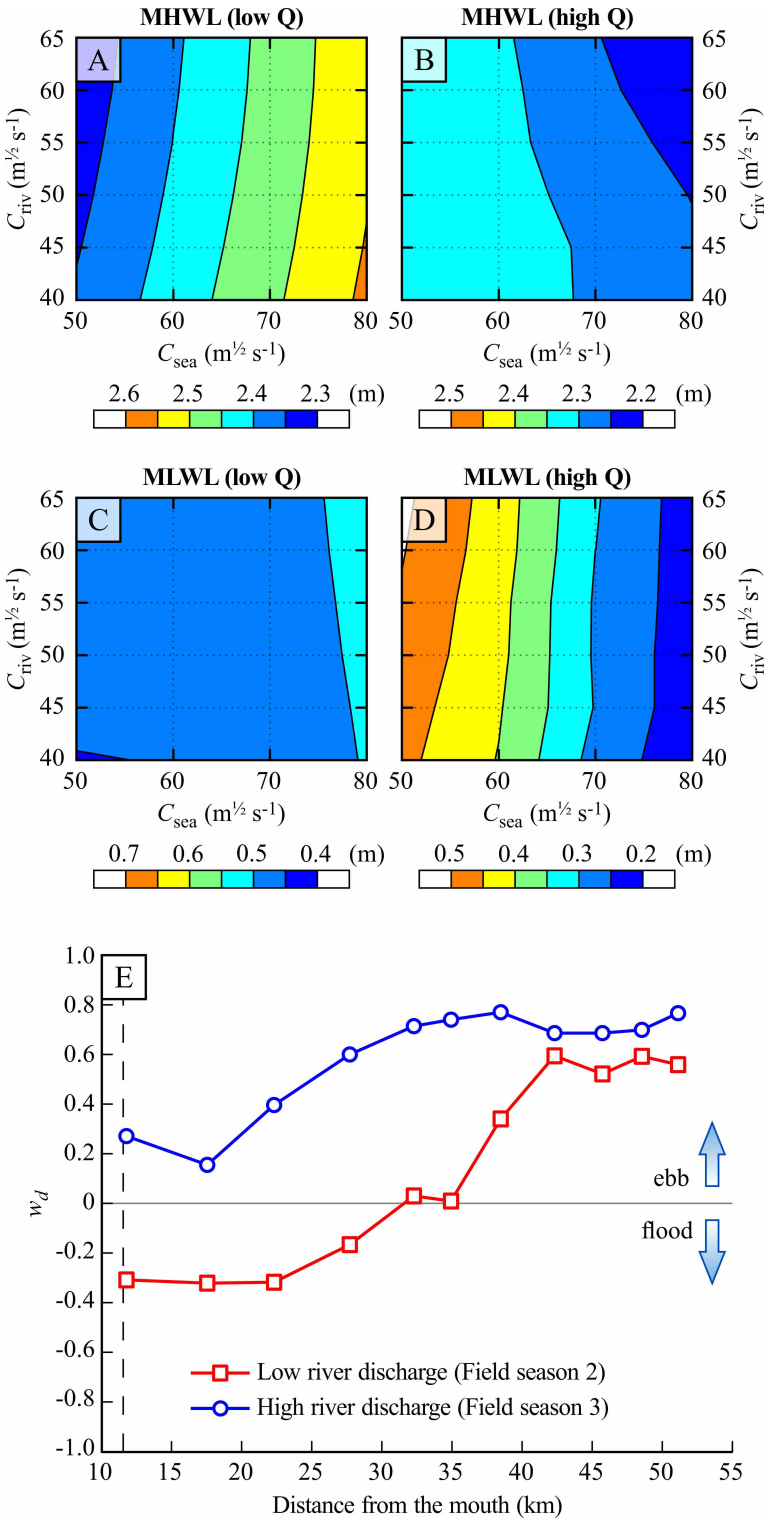

340

341 **Figure 3.** (A-D) Mean high and low water levels predicted by the 3D FLOW-WAVE

342 model. (E) Proportion of the total work done during flood and ebb calculated using

343 Equations [3]. Vertical dash-line denotes Hammond tide gauge.

where positive w_d indicates ebb is dominant, and negative w_d indicates flood is dominant (Figure 3E).

There is an increase in w_d in the upstream direction, as well as a clear difference in the work done during the periods of high and low river-discharge. During low river flow, the work done in the flood period dominates in the lower to middle part of the estuary, corresponding to the increased sensitivity to roughness at high water levels (flooding process). During high river flow, the ebb work-done dominates for most of the estuary, corresponding to the increased sensitivity to roughness at low water levels (ebb process).

A direct comparison between 2D estuary-boundary and 3D sea-boundary results (Figure 4) is presented relative to the Hammond water level data. These results demonstrate that the 2D estuary-boundary model performs best and this is most noticeable at the Skamokawa tide gauge.

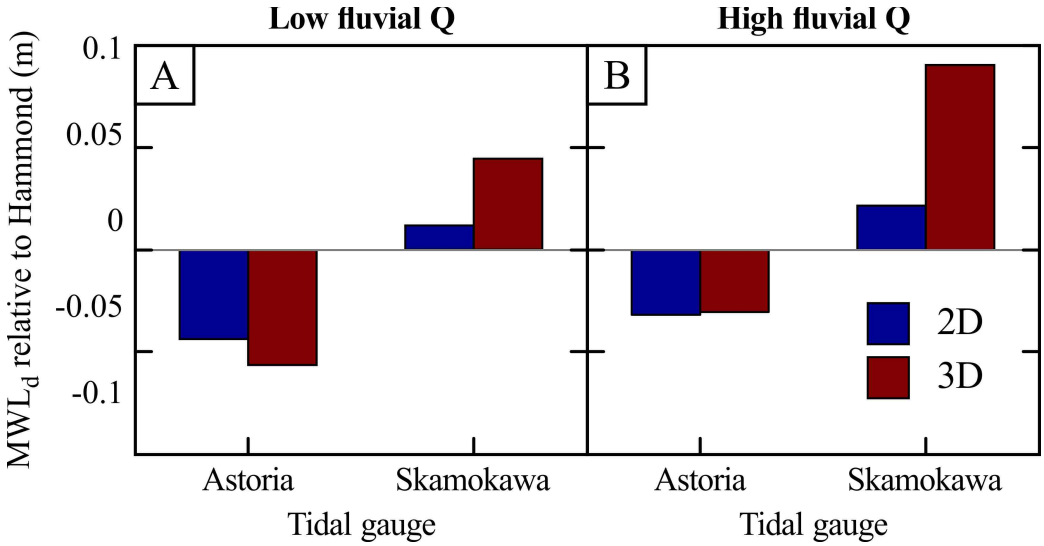

Figure 4: Difference between predicted and measured mean water level.

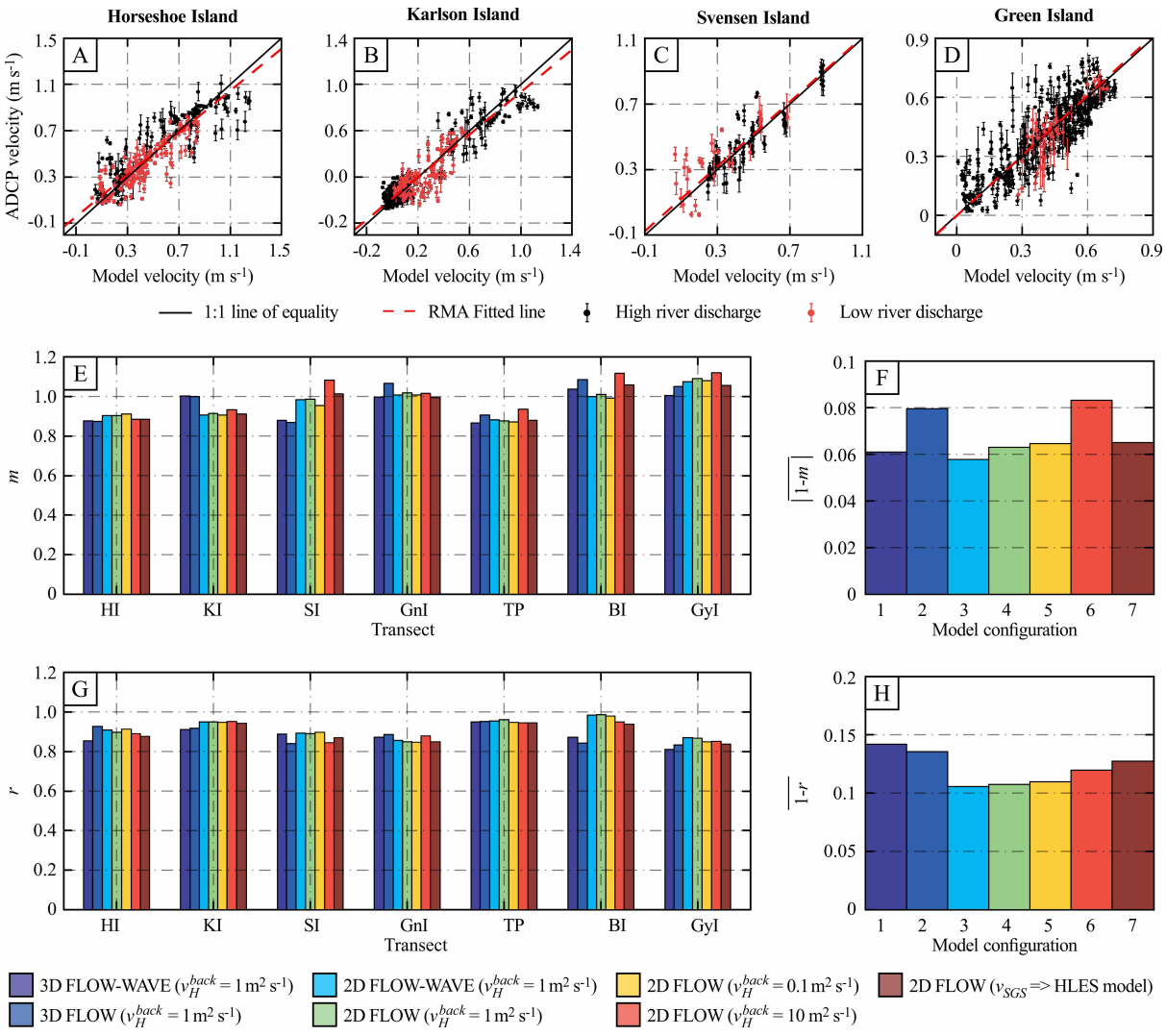

Figure 5: (A-D) Comparison between measured ADCP and predicted model (2D FLOW v_H^{back} = 1 m² s-1) velocities for four transects. Error bars represent one standard deviation from the within model-cell variability. (E & F) Gradient *m* obtained from RMA least-squares regression, (G & H) correlation coefficient.

4.2 Model validation

The salinity data were assessed using the Root Mean Square Error (RMSE), and the model skill using the Index of Agreement [Willmott, 1981]. The results from this

371 analysis are not presented here but they demonstrate: i) neither model configuration
372 (FLOW or FLOW-WAVE) systematically out-performed the other; ii) the model skill is
373 higher in the lower part of the estuary, a result also observed by Elias et al. [2012]; and
374 iii) the present model performs to a similar level of accuracy as other modelling studies
375 of the CRE [Elias et al., 2012; Kärnä et al., 2015; Kärnä and Baptista, 2016].
376
377 Although it is possible to obtain the non-stationary amplitude and phase [Matte et al.,
378 2013], herein we use the t_tide Matlab toolbox [Pawlowicz et al., 2002] since the
379 analysis window is one month. The 2D and 3D configurations (case 1 and 3: Table 1)
380 and observations were analysed (Table 2).
381
382 Both model configurations reproduce the tidal amplitudes to a similar level of accuracy:
383 the average and maximum amplitude errors being 0.01 m and 0.05 m respectively. The
384 2D estuary-boundary model performs slightly better at reproducing the tidal phase with
385 an average/maximum phase error of around $3/5^{o}$ compared to $7/12^{o}$ for the 3D sea-
386 boundary configuration. The results also show that the amplitudes are damped by
387 increasing river discharge for M_2, S_2 and O_1 but amplified for K_1. The components that
388 are effected most are K_1 and S_2.
389
390 We have also computed the model skill and absolute error (Table 3). The results show
391 that the RMSE is relatively large for the 3D case. This maybe surprising given the
392 amplitude and phase differences between these configurations is small. This is due to
393 poor representation of the MWL as discussed in section 4.1 and demonstrated in
394 Figures 2A and 2B.

In Figures 5A–5D, a direct comparison between the modelled and measured velocity magnitude is given for four ADCP transects with error bars for variability. The degree of bias is illustrated using the line fitted using Reduced Major Axis (RMA) linear regression (compare with the 1:1 line of equality). In Figure 5E, the RMA gradient for each transect and model configuration is shown. The average of the absolute difference between 1 and the computed gradient ($|\overline{1-m}|$) across all transects is shown in Figure 5F. The degree of scatter is quantified here using the correlation coefficient *r* (Figure 5G). The mean difference between a perfect correlation coefficient of 1 and the actual correlation coefficients ($\overline{1-r}$) are presented in Figure 5H. These results show that the 2D estuary-boundary model with uniform viscosity ν_H^{back} = 1 m^2 s^{-1} performs best.

	Amplitude (m)											
Gauge	**M_2**			**K_1**			**S_2**			**O_1**		
Station	Obs	2D	3D	Obs	2D	3D	Obs	2D	3D	Obs	2D	3D
Ham	0.95 *0.91*	- -	0.95 *0.95*	0.31 *0.49*	- -	0.29 *0.49*	0.30 *0.17*	- -	0.32 *0.20*	0.25 *0.24*	- -	0.24 *0.23*
Ast	1.01 *0.96*	0.97 *0.91*	1.02 *0.97*	0.30 *0.47*	0.29 *0.46*	0.30 *0.46*	0.30 *0.16*	0.30 *0.16*	0.32 *0.18*	0.23 *0.22*	0.23 *0.21*	0.24 *0.21*
Ska	0.88 *0.79*	0.89 *0.79*	0.92 *0.79*	0.26 *0.37*	0.24 *0.38*	0.24 *0.36*	0.24 *0.13*	0.27 *0.13*	0.29 *0.13*	0.18 *0.15*	0.19 *0.16*	0.19 *0.15*
	Phase (Degrees)											
Gauge	**M_2**			**K_1**			**S_2**			**O_1**		
Station	Obs	2D	3D	Obs	2D	3D	Obs	2D	3D	Obs	2D	3D
Ham	75	-	69	192	-	186	27	-	21	112	-	104

	234	-	*228*	*126*	-	120	41	-	*31*	346	-	*339*
Ast	87	89	81	198	201	192	41	44	34	115	120	108
	247	*250*	243	*133*	*137*	*130*	*61*	63	49	357	1	356
Ska	114	112	106	220	217	209	72	69	61	134	135	125
	279	*280*	*276*	153	*158*	*154*	*93*	*92*	80	*34*	*32*	34

Table 2: Modelled and measured tidal amplitude and phase for the low (field-season 2, roman) and high (field-season 3, italics) discharge periods.

Gauge	**IOA**				**RMSE (m)**			
	field-season 2		field-season 3		field-season 2		field-season 3	
	2D	3D	2D	3D	2D	3D	2D	3D
Ham	-	0.979	-	0.979	-	0.22	-	0.23
Ast	0.998	0.985	0.998	0.979	0.07	0.20	0.07	0.24
Ska	0.998	0.964	0.998	0.982	0.06	0.28	0.06	0.18

Table 3: Index of agreement and root mean square error computed for the low (field season 2) and high (field season 3) discharge periods.

4.3 Hydrodynamics and morphodynamics in the TIFZ

The 2D estuary-boundary model results (from configuration 3 in Table 1) were used to investigate the channel scale hydrodynamics and morphodynamics in the TIFZ of the CRE. This is the best performing configuration based on our analysis. To begin, small regions (1.1 and 1.2, Figure 1) are used to investigate temporal flow patterns, total

sediment transport and the contribution of tidal and fluvial forcing. These results are then used to generalise the results in the upper part of the CRE (region 2, Figure 1).

4.3.1 Temporal flow patterns in region 1.1

The flow patterns during a high discharge period (field season 3, Table 1) where the flow changes from ebb to flood in region 1.1 (Figure 1B) are presented in Figure 6. This region includes the Grassy Island ADCP transect (Figure 1B). Measured and modelled data from three time periods are shown in Figures 6G-6I.

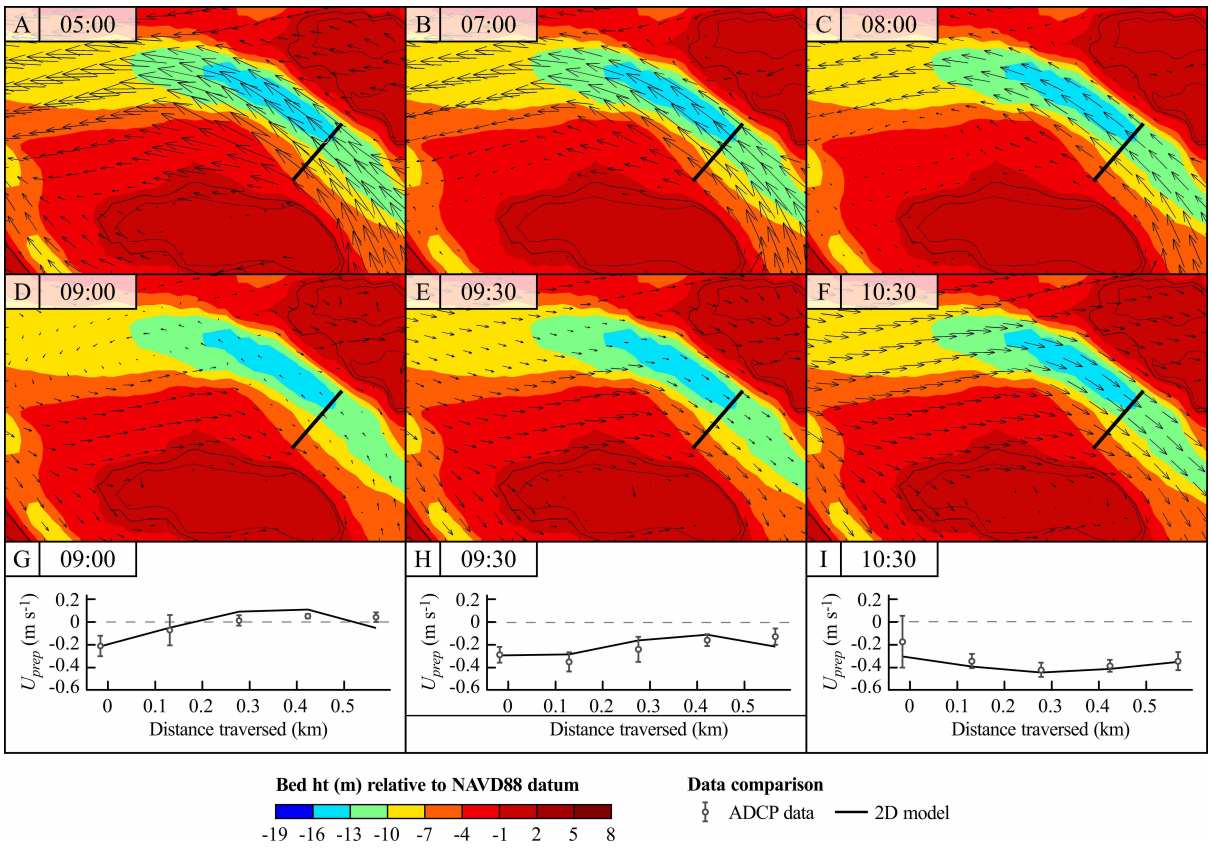

Figure 6: Series of model and ADCP data showing the flow within a channel and across the Grassy Island transect (Figure 1B) on the 18th June 2012 PST in region 1.1 (Figure 1B).

In Figure 6A, the velocities are ebb-directed and approximately at maximum magnitude. During the next two hours, the velocity magnitude is reduced (Figure 6B), and one hour later (Figure 6C) the flow remains predominately ebb-directed, although some of the flow has reversed and a recirculation zone develops.

In the following hour, nearly all the flow has reversed (Figure 6D). In the Prairie Channel (Figure 1B), the flow is flood-directed in the shallow areas but remains ebb-directed in the deeper part of the channel. This bidirectional flow pattern is exhibited in both the measured and modelled data (Figure 6G) and the recirculation zone is still evident (Figure 6D). The recirculation is driven by opposing ebb-directed flow from the Prairie Channel and flood-directed flow from downstream. Thirty minutes later (Figure 6E), the flow in this area is entirely ebb-directed, with the velocity magnitude in the shallow areas being much greater than in the deeper part of the channel. The flow profiles illustrate this also (Figure 6H). Finally, one hour later (Figure 6F and 6I), the flow velocities in the deeper part of the channel are now greater than in the shallow areas.

The flow in this region is affected by both tidal and fluvial flows, as well as a clear influence of bed topography. Analysis of the results showed that the flow duration is flood-biased in some areas of this region, typically along the margins of the channel and in the lee of Grassy Island (with respect to the ebb direction). The same general flow patterns are observed during the low discharge period although the magnitudes of the ebb flow velocities and duration are reduced.

458

459 **4.3.2 Sediment transport in region 1.2**

460

461 The influence of tidal and fluvial forcing, combined with bathymetric variability, may
462 lead to mean flood-directed flow. This is demonstrated for a slightly larger area (region
463 1.2, Figure 1B) than outlined in the previous section. To compute the mean flow
464 direction, the model was run in a steady configuration using mean water level height
465 and discharge at the model boundaries. This was used to define a directional parameter
466 d (= ±1) to denote ebb- (d = +1) or flood- (d = -1) directed flow: $d = \boldsymbol{U} \cdot \boldsymbol{U_s} / |\boldsymbol{U} \cdot \boldsymbol{U_s}|$,
467 where $\boldsymbol{U}$ and $\boldsymbol{U_s}$ are the 2-dimensional horizontal velocity vectors from the unsteady
468 and the steady model configurations respectively.

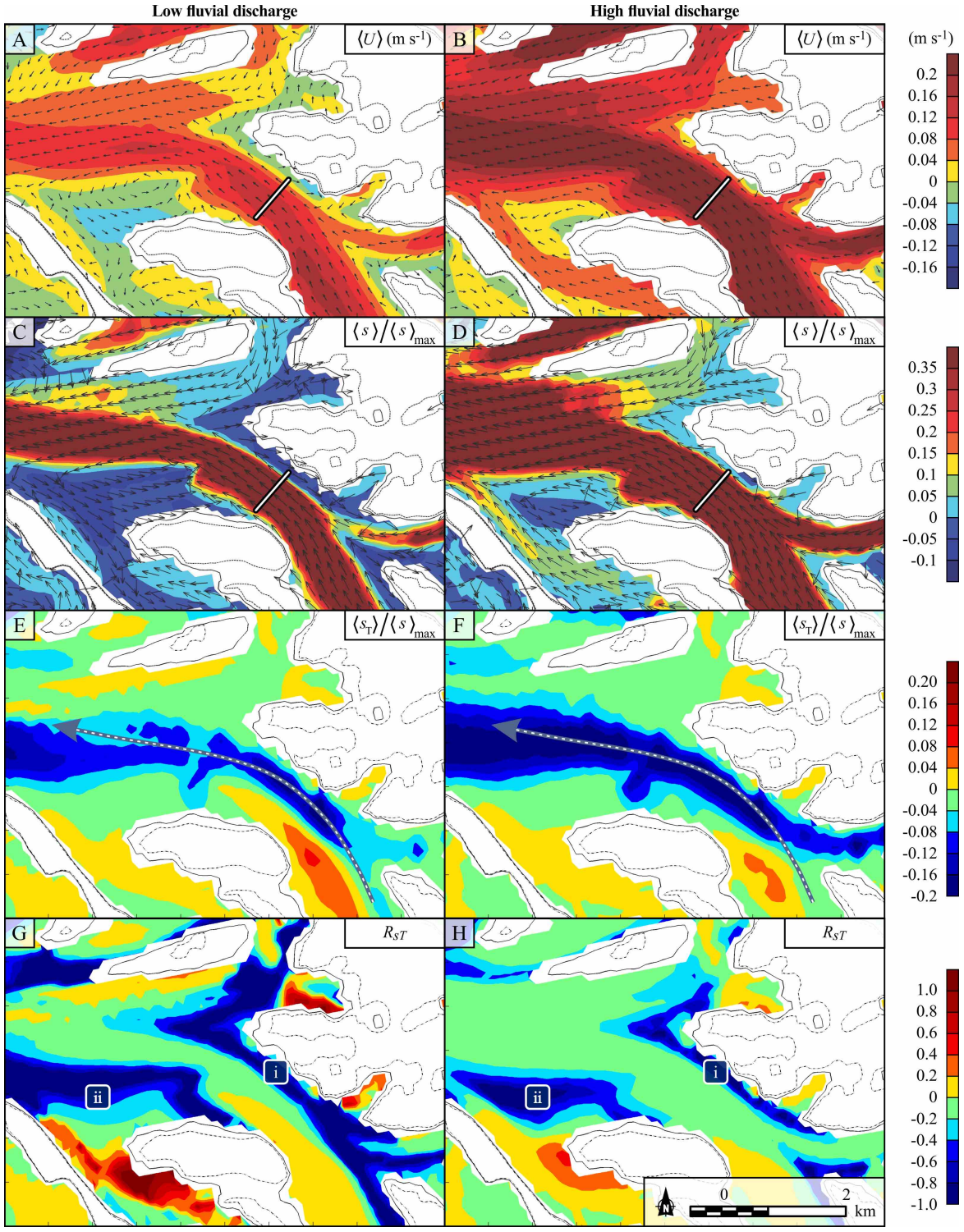

469

470 **Figure 7:** Tidal averaged flow in region 1.2 defined in Figure 1. (A & B) velocity and (C &
471 D) total sediment transport, (E & F) tidally-variable sediment transport, (G & H) tidally-
472 variable sediment transport ratio. ($\langle s \rangle_{max}$ = 0.0576 m^5 s^{-5} local maximum during low
473 river-discharge).

474 The direction parameter was then used to scale the velocity magnitude to separate ebb-
475 and flood-directed flow velocities and time-averaged across a lunar cycle (denoted
476 using angled braces). The results of the analysis (Figures 7A and 7B; vector length does
477 not represent magnitude), show that regions of ebb-directed net flow exist with
478 velocities greater than 0.04 m s^{-1} (Figure 7A). Zones of flood-directed net flow are
479 observed in the lee of Grassy Island and along the channel margin (Figure 7A).
480 Increasing the river-discharge reduces the extent of these zones (Figure 7B) and
481 increases maximum tidal-averaged velocity (from 0.18 m s^{-1} to 0.29 m s^{-1}).
482
483 These results indicate that there is potential for net sediment transport in this region. In
484 principle, the sediment transport rate may be computed directly using a sediment
485 transport scheme. However, application of these schemes requires careful site-specific
486 calibration. For simplicity, the Engelund and Hansen [1967] transport scheme is used
487 herein. A proxy for sediment transport denoted with a lowercase s (= U^5). For the
488 remainder of this paper, this is referred to as the sediment transport capacity. A similar
489 approach has been adopted by others [e.g. Hoitink et al., 2003; Van Maren et al., 2004].
490
491 The sediment transport capacity was time-averaged over a lunar tide. The results are
492 presented (Figures 7C and 7D) as a fraction of local maximum tidal-averaged sediment
493 transport capacity $\langle s \rangle_{\max}$ evaluated within region 1.2 (vectors denote the time-averaged
494 direction) from the low discharge period.
495
496 During the high discharge period (Figure 7D), sediment transport is nearly entirely ebb-
497 directed with only small regions of flood-directed transport, in particular in the lee of

Grassy Island. In the Prairie Channel, the ebb-directed transport is greater than the range of contours presented, except for some areas close to the channel margin. During the low discharge period (Figure 7C), sediment transport remains principally ebb-directed. In the lee of Grassy Island, and in some margins of the Prairie Channel, there are regions of flood-directed sediment transport with magnitudes greater than 5% of the local maximum. These regions of flood-directed transport have a larger spatial extent than the tidal-averaged velocity.

4.3.3 Tidal analysis of sediment transport in region 1.2

To understand the principal factors driving these flow and sediment transport patterns, the flood and ebb-directed velocity magnitude were further analysed. The full signal is split into mean (U_0) and tidally-variable (U_T) velocities: $U = U_0 + U_T$. To do this: the tidally-variable part was computed using the t_tide Matlab toolbox [Pawlowicz et al., 2002] and the mean component obtained from the difference between the total and the tidally-variable ($U_0 = U - U_T$). Using these reconstructed velocities, the mean (s_0) and tidally-variable (s_T) sediment transport capacities were computed.

The sediment transport capacities show that the tidally-variable part (s_T) is significantly larger than the mean part (s_0) which is typically ebb-directed. In Figures 7E and 7F the tidally-variable sediment transport capacities are presented scaled by $\langle s \rangle_{max}$ = 0.0576 $m^5\ s^{-5}$. The tidally-variable part (s_T) is typically flood-directed with similar spatial distribution for both high and low discharge periods. The largest s_T values are aligned

along the Prairie channel (denoted with dashed arrow) where water depths are largest in region 1.2.

To compare the total and reconstructed sediment transport capacities, we define the following ratios:

$$R_{sT} = \langle s_T \rangle / |\langle s \rangle| \,, \quad R_{s0} = \langle s_0 \rangle / |\langle s \rangle| \,. \qquad [2]$$

Negative values indicate flood-directed sediment transport.

The spatial distribution of R_{sT} are similar for both flow periods (Figures 7G and 7H). The sediment transport is flood-directed and large compared to the total transport: i) along the north margin of the Prairie Channel and ii) in the layer between the Prairie Channel and the lee of Grassy Island.

Along the north margin of the Prairie Channel (i), the tidally-variable sediment transport appears to be the principal mechanism that results in flood-directed sediment transport.

Across the layer between the Prairie Channel and the lee of Grassy Island (ii), the total sediment transport capacity transitions from ebb-directed (within the Prairie Channel) to flood-directed (in the lee of Grassy Island) sediment transport. The large R_{sT} magnitude in this region is a result of relatively small total sediment transport due to competing tidal and mean flow. In the lee of the bar, the tidally-variable and mean flow

545 sediment transport capacities are flood-directed (not shown) and so the total sediment
546 transport capacity is flood-directed.
547
548 **4.3.4 Tidal analysis of sediment transport in region 2**
549
550 In Figures 8A and 8B, the tidally-variable sediment transport ratio (R_{sT}) are presented
551 for the upper to mid part of the estuary (region 2 – Figure 1). Similar patterns are
552 observed to those discussed previously. To compare these two ratios directly, the
553 difference (R_{sT} - R_{s0}) is calculated and presented in Figures 8C and 8D.
554
555 Analysis of the data showed that the dominant constitutes are O_1 and M_2 for the low and
556 high discharge periods respectively. The second largest constitute is K_1 for both
557 discharge periods. Hoitink et al. [2003] showed that the linear interaction between
558 these components (K_1, M_2 and O_1) results in tidal asymmetry. They formulated
559 analytical expressions to compute sediment transport (velocity raised to 3rd or 5th
560 power). These formulations show that the long-term average sediment transport
561 depends only on the amplitude and phase of these constitutes.
562
563 To test these formulations in the CRE, we computed the sediment transport (5th power)
564 using the obtained tidal components and Hoitink's formulation. The sediment transport
565 patterns are very different to the sediment transport patterns computed using the time
566 series data (not shown). In the CRE, the fluvial discharge is not negligible so the
567 sediment transport capacity was also computed using the mean flow (M_0) combined
568 with the same constitutes as Hoitink et al. [2003] (K_1, M_2, O_1, M_4). The resultant

569 sediment transport patterns (not shown) are very similar to the results obtained using
570 the original time series (Figures 8E and 8F). We also tested with the Van Maren et al.
571 [2004] formulation and similarly found that the sediment transport (this time 3rd
572 power) computed using time series data and reconstructed from components (M_0, K_1,
573 M_2, and O_1) were very similar.
574

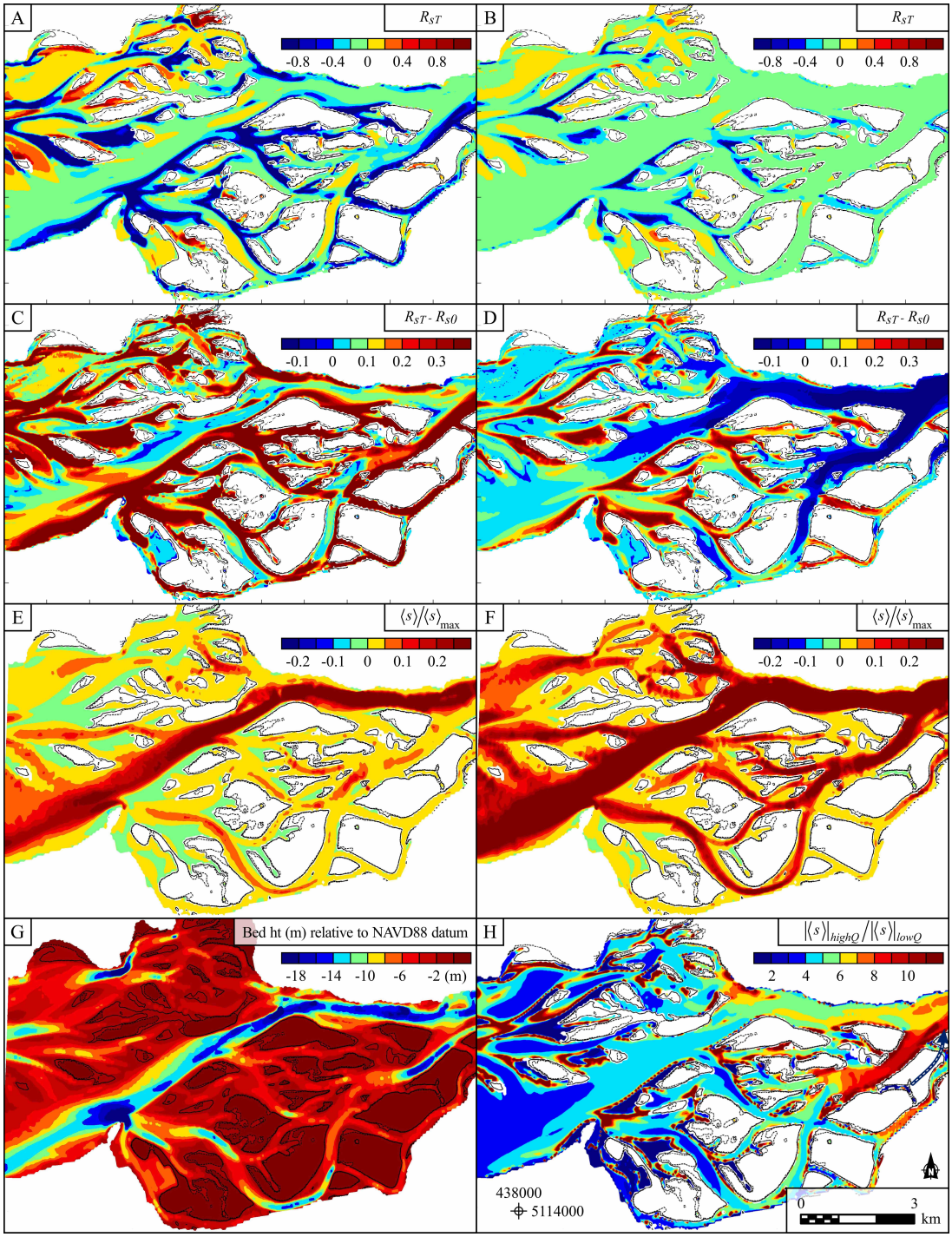

575

576 **Figure 8:** Tidal average sediment transport in area 2. (A & B) tidally-variable sediment
577 transport ratio, (C & D) difference between sediment transport ratios, (E & F) total
578 sediment transport ($<s>_{max}$ = 0.5065 m^5 s^5 from the low discharge period), (G) bed level
579 relative to NAVD88 and (H) ratio of the sediment transport from high and low discharge
580 periods.

4.3.5 Net sediment transport in region 2

Calculated sediment transport capacities are presented In Figures 8E and 8F. The bed topography in this region is presented in Figure 8G for reference. For the area presented, $\langle s \rangle_{\max}$ = 0.5065 and 2.6324 m^5 s^{-5} for the low and high discharge periods respectively. The maximum sediment transport capacities were obtained in the Navigation Channel in the upper part of the estuary.

In both the north and south embayments, most locations exhibit ebb-directed sediment transport around $0.05\langle s \rangle_{\max}$ or less. In the remaining locations, small magnitude flood-directed and larger magnitude ebb-directed sediment transport is observed. The larger magnitude ebb-directed transport is concentrated in the deeper scoured areas. During low river flow periods (Figure 8E), large regions of flood-directed sediment transport are observed in the lee of the bars and islands. Flood-directed sediment transport along the margins of the channels is also evident.

Finally, the ratio of sediment transport from the high and low river flow periods was computed (Figure 8H). Sediment transport ratios greater than (less than) one indicate areas of increased (reduced) sediment mobility. The results show that this ratio is greater than one for most (92%) of the area presented. The ratio is spatially-variable with the largest values (~ 5) being located near the head of the estuary, and reducing along the axis of the estuary seaward (~ 2.5).

5. Discussion

605

606 The model calibration results presented herein highlight an inversion of the 3D model
607 roughness sensitivity to water level variations due to a change in river-discharge. This
608 was attributed to a change in the amount of work done during the two discharge
609 periods. However, the 2D model did not exhibit this behaviour because the bed shear
610 stress is related to the bulk momentum of the entire column in the 2D model rather than
611 being explicitly resolved.

612

613 From analysis of salinity and water level data (not shown), we found that the 3D sea-
614 boundary model performed to a similar level of accuracy compared to other models
615 [Elias et al., 2012; Kärnä et al., 2015; Kärnä and Baptita 2016] of the CRE. Our results
616 also demonstrated that the 2D estuary-boundary configuration performed better than
617 the 3D sea-boundary configuration in terms of calibration and validation statistics. This
618 was based on analysis of observed water-level and flow data. This may be due to
619 modelling more complex system including coastal and mouth processes and
620 demonstrates the difficulties associated with modelling the CRE. One particular
621 difficulty is related to the specification of the seaward boundary. The approach adopted
622 herein and by Elias et al. [2012], the sea boundary height is specified using stationary
623 mean water level. The associated error in the estimation of this height is 0.226 m
624 (VDatum: http://vdatum.noaa.gov/docs/est_uncertainties.html). In the 2D estuary-
625 boundary simulations, the water levels are specified using measured data, and the
626 model boundary conditions are therefore more constrained. Our results suggest that,
627 although stratification and vertical process representation are important, similar if not

628 better model predictions can be obtained using a 2D model constrained within the
629 estuary.
630
631 The differences in performance may also be due to running the 3D model at lower
632 resolution. As a test, we ran additional simulations at the lower resolution for the 2D
633 case. Reducing the resolution results in slightly poorer calibration and validation
634 statistics although the differences are small [not shown]. We therefore expect that the
635 3D model calibration and validation statistics to be only marginally better if run at
636 higher resolution.
637
638 The temporal and spatial flow data show that larger peak velocities are associated with
639 the deeper areas of the channels, likely due to topographic forcing. The associated
640 increase in momentum results in a greater lag in response to water-level change
641 compared to comparatively slower flow in the shallower and more sheltered areas. This
642 was demonstrated in an area of the south embayment (region 1.1). This results in net
643 ebb-directed flow in the deeper channels and flood-directed flow into the shallower and
644 more sheltered areas (region 1.2). Similar spatial distributions were obtained for net-
645 sediment transport capacities (region 1.2). Increasing the river-discharge results in a
646 reduction in the spatial extent of the flood-directed flow and sediment transport.
647
648 Although the sediment transport is principally ebb-directed, there are areas of net
649 flood-directed sediment transport, which has two implications for sedimentological
650 processes. Firstly, in the lee of islands and bars, flood-directed flow provides a source of
651 sediment that could subsequently be deposited, and a mechanism to extend bar/island

topography downstream. Secondly, flood-directed flow may produce flood-directed bedforms. If these bedforms are preserved in bar/island stratigraphy, they could provide a signature that may help interpret the origin and evolution of depositional forms in the TIFZ. However, their preservation potential is also linked to aggradation rate, and thus in regions of large amplitude gross-, but low amplitude net-, sediment transport, the bedforms produced are likely to be more symmetrical. Such a situation is observed at the margins of Prairie Channel and in the lee of Grassy Island during high river-discharge. At the same time, large ebb-directed sediment transport will likely produce ebb-directed bedforms. This yields the potential for spatial variations in the degree of bedform symmetry and therefore the potential difficulty in associating certain bedform assemblages with a downstream position in the fluvial-tidal zone [Venditti et al., 2012].

To better understand the principal driving mechanism for flood- and ebb-directed sediment transport, the tidal signal was split into tidally-variable and mean parts. To compare the influence of each, two parameters were used: R_{sT} and R_{s0} (Equation 2). The tidally-variable part (R_{sT}) is principally flood-directed, large compared to R_{s0} and spatially variable. In particular, large negative (flood-directed) R_{sT} is observed in two locations: i) along the margin of the channels where tidal variability is the main mechanism for flood-directed sediment transport (R_{s0} is typically ebb-directed); and ii) areas where the principal net sediment direction changes (in the lee of bar topography), this highlights areas where the mean part is also negative. The converse is true for the mean part R_{s0} (not shown). In region 2, R_{s0} is fairly uniform and generally small compared to $\langle s \rangle$ during the low discharge period. However, during the high discharge

676 period, R_{s0} exhibits greater variability increasing in magnitude towards the head of the
677 estuary. Furthermore, direct comparison between these parameters shows that the
678 tidally-variable ratio is dominant - in particular during the low discharge period and in
679 the channel margins.
680
681 Although R_{s0} is generally small compared to R_{sT}, the mean component is crucial in
682 determining the resultant sediment transport patterns. This was observed in tests
683 where the resolved constituents without the mean flow (M_0) were used to reconstruct
684 the sediment-transport (not shown here). Furthermore, given K_1, M_2 and O_1 are the
685 dominant constituents in the CRE and have previously been linked to tidal asymmetry
686 [Hoitink et al., 2003], we also tested the following combination: K_1, M_2, O_1, M_4 pus M_0.
687 The spatial sediment transport patterns were computed by reconstructing the flow
688 from the given constitutes. The reconstructed sediment transport patterns are visually
689 similar to the total sediment transport, and demonstrates the importance of the mean
690 flow in determining the sediment transport patterns in the CRE. This was also
691 demonstrated by Chu et al. [2015] who found that the mean flow can modify the
692 temporal and therefore long-term transport patterns.
693
694 The impact of river-discharge on the sediment transport patterns in the CRE is
695 dominated by three factors. Firstly, due to topographic forcing, river-discharge is
696 preferentially routed into deeper parts of the channels. This results in ebb-dominance in
697 the deeper channels. Flood-dominance is still possible, and was demonstrated in the
698 shallow and sheltered areas, but increasing river-discharge limits the spatial extent of
699 the flood-directed areas. Secondly, although the magnitude of the mean flow can be

700 small, its effect on determining the sediment transport patterns is significant. Finally,
701 the effect of increasing the discharge leads to increased sediment transports.
702
703 # 6. Conclusions
704
705 Delft3D was applied to simulate the hydrodynamics of the Columbia River Estuary, with
706 testing of two modelling configurations and parameter sensitivity. The models were
707 calibrated using water level data and validated using salinity and flow data. Overall, the
708 model performs very well at reproducing the measured water levels and flow patterns.
709 Our results show that a 2D estuary-boundary model can be used to provide a good
710 representation of planimetric hydrodynamics within a highly energetic and stratified
711 estuary.
712
713 A detailed description of the flow within an area of the south embayment illustrates the
714 complex interactions between hydrodynamic forcing of the tidal flood with the
715 momentum of the ebb-directed flow during the turn of the tide. Flow reversals occur
716 first in areas sheltered by bar/island topography and along the margins of the channels,
717 thereby producing planimetric bidirectional flows and recirculation zones.
718
719 These interactions result in net sediment transport that is principally ebb-directed.
720 However, within the channels and sheltered areas, flood-directed flow and sediment
721 transports are evident. The results indicate that this is due to topographic forcing that
722 focuses most of the river-discharge into deeper parts of the channels. Increasing the
723 river-discharge results in a reduction of the extent of the flood-directed flow and

724 sediment transport. Further analysis of the results showed that: i) flood-directed
725 sediment transport along the channel margins is due to tidal variability and ii) flood-
726 directed sediment transport in the lee of bars is due to both tidal variability and mean
727 flow.

728 **Acknowledgements**

729 We are grateful to CMOP, USGS, NOAA, USACE, LCREP and PSLC (all fully referenced
730 within the paper) for supplying bathymetric and hydrological data critical to the model
731 application. Calculations for this study were performed using the University of Exeter
732 Supercomputer. This research was funded by UK Natural Environment Research
733 Council (NERC) on a split grant award with reference numbers: NE/H007954/1,
734 NE/H006524/1, NE/H007261/1 and NE/H00582X/1. Fieldwork was made possible by
735 access to the extensive facilities at the Clatsop Community College Marine and
736 Environmental Research and Training Station; we thank in particular António Baptista,
737 Michael Wilkin and Katie Rathmell for their help in servicing equipment, providing
738 access to machine workshops, training in marine health and safety and provision of a
739 Humber Class RIB. Rob Strick and Greg Sambrook Smith helped obtain some of the field
740 data. Finally, we thank Pat Killion for his navigation skills on the Tansy Point and
741 essential local expertise in the ever-changing conditions in the Columbia River Estuary.

742

743

744 # References

745

746 Achete, F.M., M. van der Wegen, D. Roelvink, and B. Jaffe (2016) Suspended sediment
747 dynamics in a tidal channel network under peak river flow, Ocean Dynamics, 66(5),
748 703-718, doi:10.1007/s10236-016-0944-0.

749 Alebregtse, N.C. and H.E. de Swart (2016) Effect of river discharge and geometry on tides
750 and net water transport in an estuarine network, an idealized model applied to the
751 Yangtze Estuary, Continental Shelf Research, 123, 29-49,
752 doi:http://dx.doi.org/10.1016/j.csr.2016.03.028.

753 Baptista, A.M., Y. Zhang, A. Chawla, M. Zulauf, C. Seaton, E.P. Myers, J.K., M.Wilkin, M.
754 Burla, and P.J. Turner (2005), A cross-scale model for 3D baroclinic circulation in
755 estuary-plume-shelf systems: II. Application to the Columbia River, Continental Shelf
756 Research, 25(7-8), 935-972, doi:10.1016/j.csr.2004.12.003.

757 Bolle, A., Z.B. Wang, C. Amos, and J. De Ronde (2010), The influence of changes in tidal
758 asymmetry on residual sediment transport in the Western Scheldt, Continental Shelf
759 Research, 30(8), 871-882, doi:10.1016/j.csr.2010.03.001.

760 Bowers, D.G., and A. Al-Barakati, (1997), Tidal Rectification on Drying Estuarine
761 Sandbanks, Estuaries, 20(3): 559-568, doi:https://doi.org/10.2307/1352614.

762 Burla, M., A.M. Baptista, E. Casillas, J.G Williams, and D.M. Marsh (2010), The influence of
763 the Columbia River plume on the survival of steelhead (Oncorhynchus mykiss) and
764 Chinook salmon (Oncorhynchus tshawytscha): a numerical exploration, Canadian
765 Journal of Fisheries and Aquatic Sciences, 67(10), 1671-1684, doi:10.1139/F10-083.

766 Chu, A., Z.B. Wang and H.J. de Vriend (2015), Analysis on residual coarse sediment
767 transport in estuaries, Estuarine Coastal and Shelf Science, 163, 194-205,
768 doi:10.1016/j.ecss.2015.06.003.
769 Dalrymple, R.W., and K. Choi (2007), Morphologic and facies trends through the fluvial-
770 marine transition in tide-dominated depositional systems: A schematic framework for
771 environmental and sequence-stratigraphic interpretation, Earth Science Reviews, 81(3-
772 4), 135-174, doi:10.1016/j.earscirev.2006.10.002.
773 Deltares (2011a), Delft3D-FLOW: Simulation of multi-dimensional hydro- dynamic
774 flows and transport phenomena, including sediments—User Manual, version: 3.15,
775 revision 14499, report, Delft, Netherlands.
776 Deltares (2011b), Delft3D-WAVE: Simulation of short-crested waves with SWAN—User
777 Manual, version: 3.04, revision 13322, report, Delft, Netherlands.
778 Díez-Minguito, M., A. Baquerizo, M. Ortega-Sánchez, G. Navarro, and M.A. Losada (2012),
779 Tide transformation in the Guadalquivir estuary (SW Spain) and process-based
780 zonation, Journal of Geophysical Research, 117, C03019, doi:10.1029/2011JC007344.
781 Dyer, K.R. (1997), Estuaries: A Physical Introduction, second edition, John Wiley and
782 Sons, Chichester, UK.
783 Elias, E.P.L., G. Gelfenbaum and A.J. van der Westhuysen (2012), Validation of a coupled
784 wave-flow model in a high-energy setting: The mouth of the Columbia River, Journal of
785 Geophysical Research: Oceans, 117(C9), C09011, doi:10.1029/2012JC008105.
786 Engelund, F., and E. Hansen (1967), A monograph on Sediment Transport in Alluvial
787 Streams, Teknisk Forlag, Copenhagen.

788 Fain, A.M.V., D.A. Jay, D.J. Wilson, P.M. Orton, A.M. Baptista (2001), Seasonal and tidal
789 monthly patterns of particulate matter dynamics in the Columbia River estuary,
790 Estuaries and Coasts, 24(5), 770-786, doi:10.2307/1352884.
791 Friedrichs, C.T., and D.G. Aubrey (1988), Non-linear tidal distortion in shallow well-
792 mixed estuaries: A synthesis, Estuarine Coastal Shelf Science, 27, 521–545,
793 doi:10.1016/0272-7714(88)90082-0.
794 Gelfenbaum, G., and G.M. Kaminsky (2010), Large-scale coastal change in the Columbia
795 River littoral cell: an overview, Marine Geology, 273, 1-10,
796 doi:10.1016/j.margeo.2010.02.007.
797 Guo, L., M. van der Wegen, J.A. Roelvink, Q. He (2014) The role of river flow and tidal
798 asymmetry on 1-D estuarine morphodynamics, Journal of Geophysical Research: Earth
799 Surface, 119, 2315–2334, doi:10.1002/ 2014JF003110.
800 Guo, L., M. van der Wegen, D.A. Jay, P. Matte, Z.B. Wang, D. Roelvink, and Q. He (2015),
801 River-tide dynamics: Exploration of nonstationary and nonlinear tidal behavior in the
802 Yangtze River estuary, Journal of Geophysical Research-Earth Surface, 120(5), 3499-
803 3521, doi:10.1002/2014JC010491.
804 Guo, L., M. van der Wegen, Z.B. Wang, D. Roelvink, Q. He (2016) Exploring the impacts of
805 multiple tidal constituents and varying river flow on long-term, large-scale estuarine
806 morphodynamics by means of a 1-D model, Journal of Geophysical Research, 121, 1000–
807 1022, doi:10.1002/2016JF003821.
808 Hoitink, A.J.F., P. Hoekstra and D.S. van Maren (2003), Flow asymmetry associated with
809 astronomical tides: Implications for the residual transport of sediment, Journal Of
810 Geophysical Research-Oceans, 108(C10), doi:10.1029/2002JC001539.

811 Hoitink, A.J.F., and D.A. Jay (2016), Tidal river dynamics: Implications for deltas,
812 Reviews of Geophysics, 54(1), 240-272. doi:10.1002/2015RG000507.
813 Jay, D.A., B.S Giese, and C.R. Sherwood (1990), Energetics and sedimentary processes in
814 the Columbia River Estuary, Progress in Oceanography, 25(1–4), 157-174,
815 doi:https://doi.org/10.1016/0079-6611(90)90006-N.
816 Huthnance, J. M. (1973). Tidal current asymmetries over the Norfolk Sandbanks,
817 Estuarine and Coastal Marine Science, 1(1), 89-99, doi: https://doi.org/10.1016/0302-
818 3524(73)90061-3.
819 Jablonski, B.V., R.W. Dalrymple, and M. Marzo, (2016), Recognition of strong seasonality
820 and climatic cyclicity in an ancient, fluvially dominated, tidally influenced point bar:
821 Middle McMurray Formation, Lower Steepbank River, north-eastern Alberta, Canada.
822 Sedimentology, 63, 552-585, doi:10.1111/sed.12228.
823 Jay, D.A., and B.S. Smith (1988), Residual circulation in and calcification of shallow,
824 stratified estuaries, Physical processes in estuaries (Editors: J. Dronkers and W. van
825 Leussen), Springer Verlag, Berlin, 21-41.
826 Jay, D.A., and J.D. Smith (1990), Circulation, density distribution and neap-spring
827 transitions in the Columbia River Estuary, Progress in Oceanography, 25, 81-112,
828 doi:10.1016/0079-6611(90)90004-L.
829 Jay, D.A., E.D. Zaron, and J. Pan (2010), Initial expansion of the Columbia River tidal
830 plume: Theory and remote sensing observations, Journal of Geophysical Research, 115,
831 C00B15, doi:10.1029/2008JC004996.
832 Jay, D.A., K. Leffler, H.L. Diefenderfer, and A.B. Borde (2015), Tidal-fluvial and estuarine
833 processes in the lower Columbia River. I: Along-channel water level variations, Pacific

834 Ocean to Bonneville Dam, Estuaries and Coasts, 38(2), 415–433, doi: 10.1007/s12237-
835 014-9819-0.
836 Kärnä, T., A.M. Baptista, J.E. Lopez, P.J. Turner, C. McNeil, and T.B. Sanford (2015),
837 Numerical modeling of circulation in high-energy estuaries: A Columbia River estuary
838 benchmark. Ocean Modelling, 88, 54-71, doi:
839 http://dx.doi.org/10.1016/j.ocemod.2015.01.001.
840 Kärnä, T., and A.M. Baptista (2016), Evaluation of a long-term hindcast simulation for
841 the Columbia River estuary. Ocean Modelling, 99, 1-14,
842 doi:http://dx.doi.org/10.1016/j.ocemod.2015.12.007.
843 Leuven, J.R.F.W., M.G. Kleinhans, S.A.H. Weisscher, and M. van der Vegt (2016), Tidal
844 sand bar dimensions and shapes in estuaries, Earth-Science Reviews, 161, 204-223,
845 doi:https://doi.org/10.1016/j.earscirev.2016.08.004.
846 Liu, Y., P. MacCready, B.M. Hickey, E.P. Dever, P.M. Kosro, and N.S. Banas (2009),
847 Evaluation of a coastal ocean circulation model for the Columbia River plume in summer
848 2004, Journal of Geophysical Research-Oceans, 114, C00B04,
849 doi:10.1029/2008JC004929.
850 Losada, M.A., M. Díez-Minguito, and M.Á. Reyes-Merlo (2017). Tidal-fluvial interaction in
851 the Guadalquivir River Estuary: Spatial and frequency-dependent response of currents
852 and water levels. Journal of Geophysical Research: Oceans, 122(2), 847-865,
853 doi:10.1002/ 2016JC011984.
854 Matte, P., D.A. Jay and E.D. Zaron (2013), Adaptation of Classical Tidal Harmonic
855 Analysis to Nonstationary Tides, with Application to River Tides, Journal of Atmospheric
856 and Oceanic Technology, 30(3), 569-589, doi:10.1002/2014JC009791.

857 Matte, P., Y. Secretan, and J. Morin (2017a), Hydrodynamic Modeling of the St. Lawrence
858 Fluvial Estuary. I: Model Setup, Calibration, and Validation. Journal of Waterway, Port,
859 Coastal and Ocean Engineering, 143(5): 04017010, doi:10.1061/(ASCE)WW.1943-
860 5460.0000397.
861 Matte, P., Y. Secretan, and J. Morin (2017b), Hydrodynamic Modeling of the St. Lawrence
862 Fluvial Estuary. II: Reproduction of Spatial and Temporal Patterns, Journal of Waterway,
863 Port, Coastal and Ocean Engineering, 143(5): 04017011, doi:10.1061/(ASCE)WW.1943-
864 5460.0000394.
865 Parsons, D.R., P.R. Jackson, J.A. Czuba, F.L. Engel, B.L. Rhoads, K.A. Oberg, J.L. Best, D.S.
866 Mueller, K.K. Johnson and J.D. Riley (2013), Velocity Mapping Toolbox (VMT): a
867 processing and visualization suite for moving-vessel ADCP measurements, Earth
868 Surface Processes and Landforms, 38, 1244–1260, doi:10.1002/esp.3367.
869 Pawlowicz, R., B. Beardsley, and S. Lentz (2002), Classical tidal harmonic analysis
870 including error estimates in MATLAB using T-TIDE, Computers & Geosciences, 28(8),
871 929-937, doi:10.1016/S0098-3004(02)00013-4.
872 Prario, B.E., W. Dragani, D.G. Mediavilla, and E. D'Onofrio (2011), Hydrodynamic
873 numerical simulation at the mouths of the Parana and Uruguay rivers and the upper Rio
874 de la Plata estuary: A realistic boundary condition, Applied Mathematical Modelling,
875 35(11), 5265-5275, doi:10.1016/j.apm.2011.04.013.
876 Prokocki, E.W., J.L. Best, P. Ashworth, D.R. Parsons, G.H. Sambrook Smith, A.P.
877 Nicholas, C.J. Simpson, H. Wang, S. Sandbach, and C. Keevil (2015), Mid to late Holocene
878 geomorphological and sedimentological evolution of the fluvial-tidal zone: Lower
879 Columbia River, WA/OR, USA In: Ashworth, P., Best, J.L. and Parsons, D.R., (Eds.),

880 Fluvial-Tidal Sedimentology, Developments in Sedimentology Series, Elsevier,
881 Amsterdam, pp. 193-226. ISBN 9780444635297.
882 Sassi, M.G., A.J.F. Hoitink, B. de Brye, B. Vermeulen, E. and Deleersnijder (2011), Tidal
883 impact on the division of river discharge over distributary channels in the Mahakam
884 Delta, Ocean Dynamics, 61(12), 2211-2228, doi:https://doi.org/10.1007/s10236-011-
885 0473-9.
886 Szupiany, R.N., M.L. Amsler, J.L. Best, and D.R. Parsons (2007), Comparison of fixed- and
887 moving-vessel flow measurements with an aDp in a large river. Journal of Hydraulic
888 Engineering, 133(12), 1299–1309, doi:http://dx.doi.org/10.1061/(ASCE)0733-
889 9429(2007)133:12(1299).
890 Van, C.P., B. de Brye, E. Deleersnijder, A.J.F. Hoitink, M.G. Sassi, B., Spinewine, H. Hidayat
891 and S. Soares-Frazão (2016), Simulations of the flow in the Mahakam river–lake–delta
892 system, Indonesia, Environmental Fluid Mechanics, 16(3), 603-633,
893 doi:https://doi.org/10.1007/s10652-016-9445-4.
894 Van Maren, D. S., P. Hoekstra, and A.J.F. Hoitink (2004), Tidal flow asymmetry in the
895 diurnal regime: bed-load transport and morphologic changes around the Red River
896 Delta, Ocean Dynamics, 54(3-4), 424-434, doi:10.1007/s10236-003-0085-0.
897 Venditti, J.G., P.A. Nelson, J.T. Minear, J.K. Wooster and W.E. Dietrich (2012), Alternate
898 bar response to sediment supply termination, Journal of Geophysical Research-Earth
899 Surface, 117, F02039, doi:10.1029/2011JF002254.
900 Willmott, C.J. (1981) On the validation of models, Physical Geography, 2, 184-194,
901 doi:10.1080/02723646.1981.10642213.
902 Zhang, Y., A.M. Baptista, E.P. Myers (2004), A cross-scale model for 3D baroclinic
903 circulation in estuary–plume–shelf systems: I. Formulation and skill assessment,

904 Continental Shelf Research, 24, 2187–2214, doi:
905 https://doi.org/10.1016/j.csr.2004.07.021.
906 Zhang, Y., A.M. Baptista (2008), SELFE: a semi-implicit Eulerian-Lagrangian finite-
907 element model for cross-scale ocean circulation, Ocean Model, 21 (3–4), 71–96.
908 doi:10.1016/j.ocemod.2007.11.005.
909 Zhou, Z., G. Coco, M. Jimenez, M. Olabarrieta, M. van der Wegen, and I. Townend (2014),
910 Morphodynamics of river-influenced back-barrier tidal basins: The role of landscape
911 and hydrodynamic settings, Water Resources Research, 50, 9514–9535, doi:10.1002/
912 2014WR015891.